remote sensing

MDPI

Article

Enhancing Regional Quasi-Geoid Refinement Precision: An Analytical Approach Employing ADS80 Tri-linear Array Stereoscopic Imagery for Aerial Triangulation Densification and GNSS Gravity-Potential Leveling

Wei Xu [1,2,3], Gang Chen [1,*], Defang Yang [2,3], Kaihua Ding [4], Rendong Dong [5], Xuyan Ma [2,3], Sipeng Han [1,6], Shengpeng Zhang [7,8] and Yongyin Zhang [8]

[1] Key Laboratory of Geological Survey and Evaluation of Ministry of Education, China University of Geosciences (Wuhan), Wuhan 430074, China; cugxuwei@cug.edu.cn (W.X.); ddwhcg@cug.edu.cn (G.C.); yangdefang@cug.edu.cn (D.Y.); maxuyan@cug.edu.cn (X.M.); hansipeng@cug.edu.cn (S.H.)
[2] Qinghai Remote Sensing Center for Natural Resources, Xining 810001, China
[3] Geomatics Technology and Application key Laboratory of Qinghai Province, Xining 810001, China
[4] School of Geography and Information Engineering, China University of Geosciences (Wuhan), Wuhan 430074, China; khding@cug.edu.cn
[5] School of Geophysics and Geomatics, China University of Geosciences (Wuhan), Wuhan 430074, China; rendong@cug.edu.cn
[6] Research Center of Applied Geology of China Geological Survey, Chendu 610065, China
[7] College of Geographical Sciences, Qinghai Normal University, Xining 810001, China; 202147341022@stu.qhnu.edu.cn (S.Z.); hhzyy@cug.edu.cn (Y.Z.)
[8] Qinghai Basic Surveying and Mapping Institute, Xining 810001, China
* Correspondence: ddwhcg@cug.edu.cn

Contents of this file

Figures S1 to S19

Subsequent analyses were conducted on China's domestically produced GF-2 and GF-7 remote sensing imagery with a superior resolution of less than 0.7m for the years 2020, 2021, and 2022 to assess horizontal displacement deformation characteristics. The number of images for these years was 51 (Figure S1a), 52 (Figure S1b), and 49 (Figure S1c), respectively. All individual images underwent spatial tri-encryption, fusion, registration, color balancing, mosaicking, and cropping as described in Section 2.1, culminating in standardized mosaicked DOM images for the study area across different years. As evident from Figures S1a- S1c, discrepancies in coloration can be attributed to varying temporal impacts and limitations of images from different years. Given the uneven number of utilized images, the boundaries of the mosaicked images are not identical, yet the approach ensures the utmost regional consistency of images (Heid et al., 2012).

Concerning these mosaicked images from each year, a pairwise differencing method was employed, leveraging the COSI-Corr software to derive the horizontal ground deformation between 2020-2021, 2021-2022, and 2020-2022. As indicated in Figures S1d and S1f, the ground deformation in all three periods was less than 5 cm. Upon further analysis of the regional topography, it was observed that the area is desolate, arid, and uninhabited. Dominated by "hilly Yardang landforms", its climatic conditions are dry with significant wind erosion, resulting in substantial aeolian movement. Such movements, influenced heavily by the environment, manifest as irregular and unpredictable displacement directions and deformations. This underscores the fact that, in recent years horizontal shifts in the study area were minimally affected by tectonic faulting.

Citation: To be added by editorial staff during production.

Academic Editor: Firstname Lastname

Received: date
Revised: date
Accepted: date
Published: date

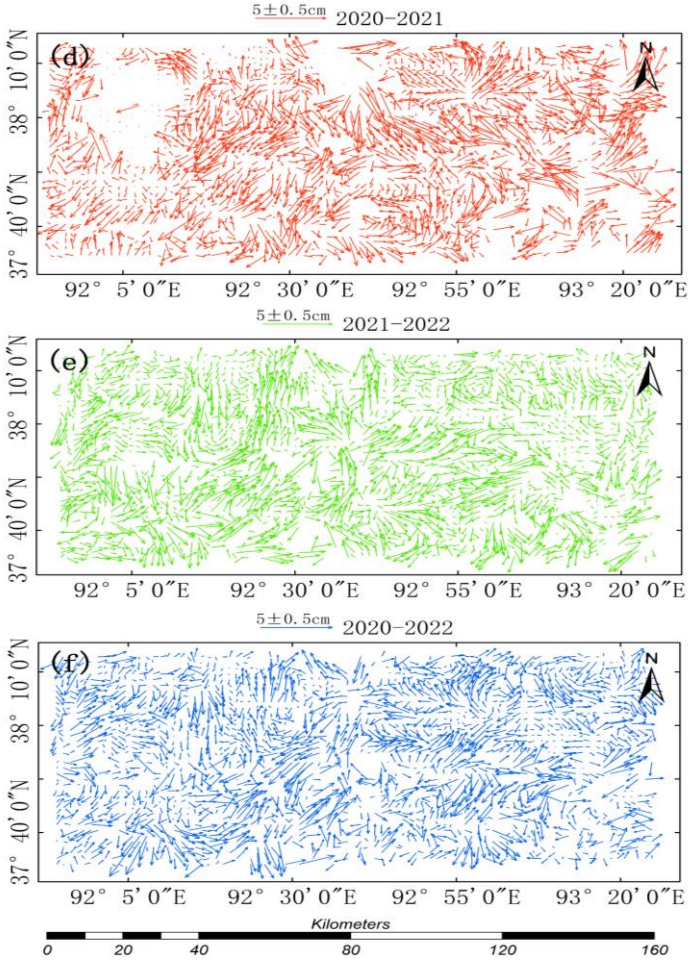

Figure S1. Precision Analysis of Height Anomalies. (a) Estimation of the Quasi-Geoid Model in the Study Area Based on GNSS-Leveling Integration. Namely (a1) - (a12) The Quasi-Geoid Models for the Study Area Fitted with Height Anomalies Calculated from Twelve Gravitational Models. (b) RMSE Values for Height Anomalies Calculated Using the Twelve Gravitational Models.

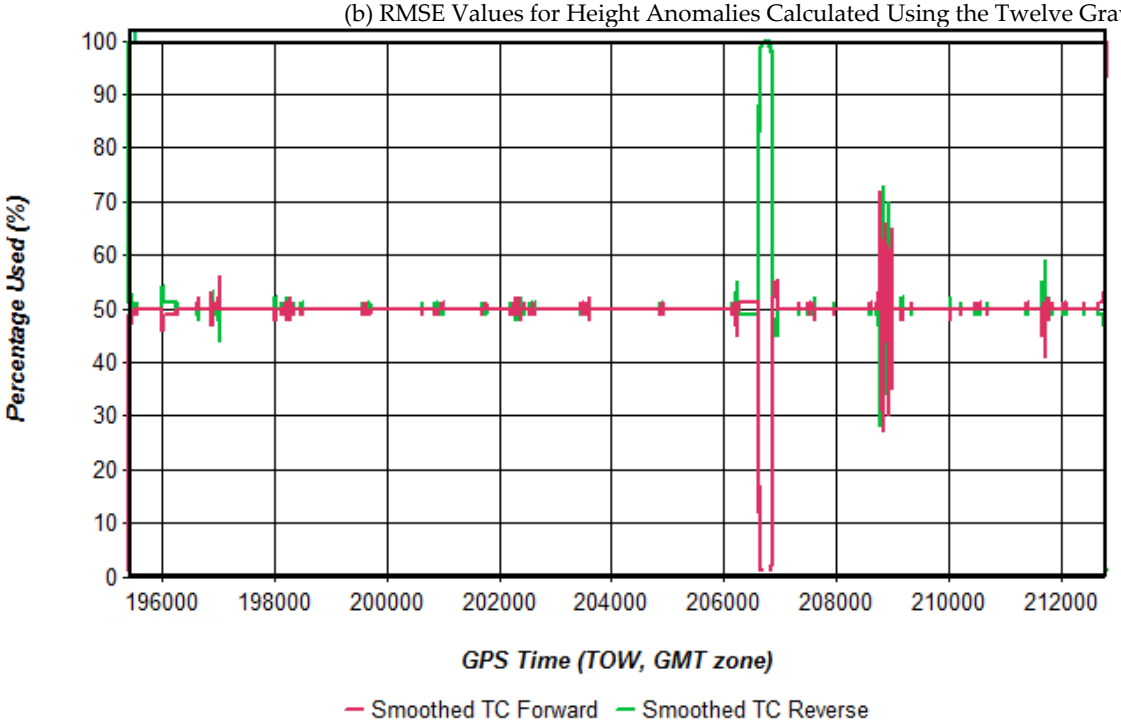

Figure S2. Both forward and reverse recursive Kalman filtering fusion.

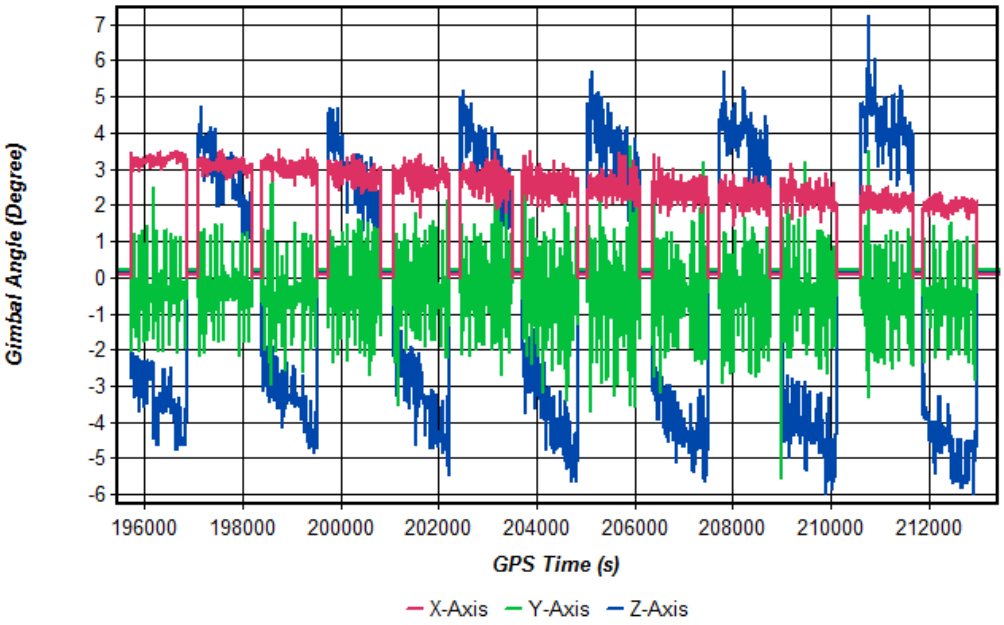

Figure S3. Correction Angles for the PAV80 Three-Axis Stabilized Platform.

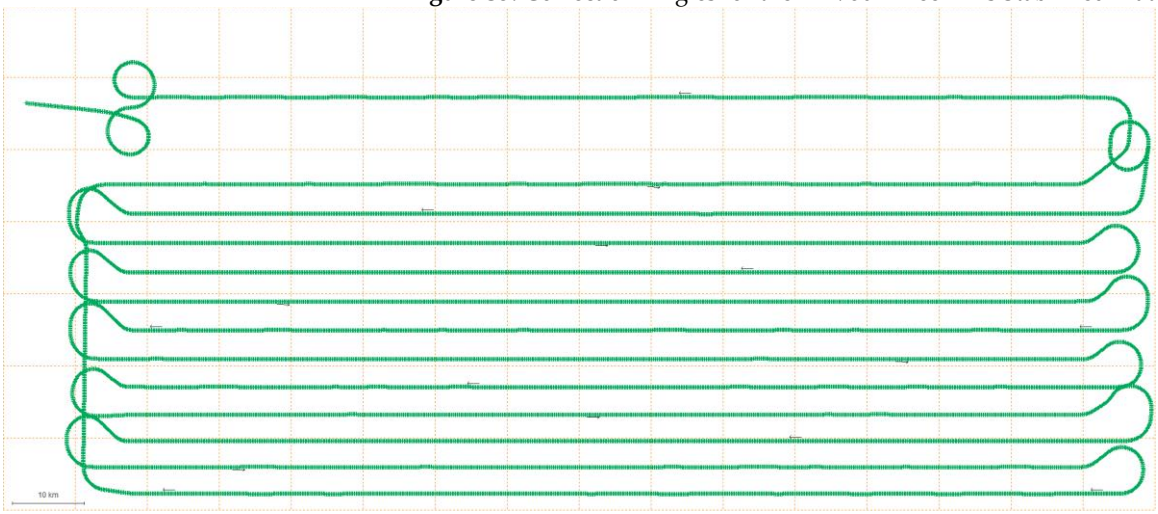

Figure S4. POS coordinates calculated from the first flight sortie. Green dots represent individual POS coordinate points, and black arrows indicate the flight direction.

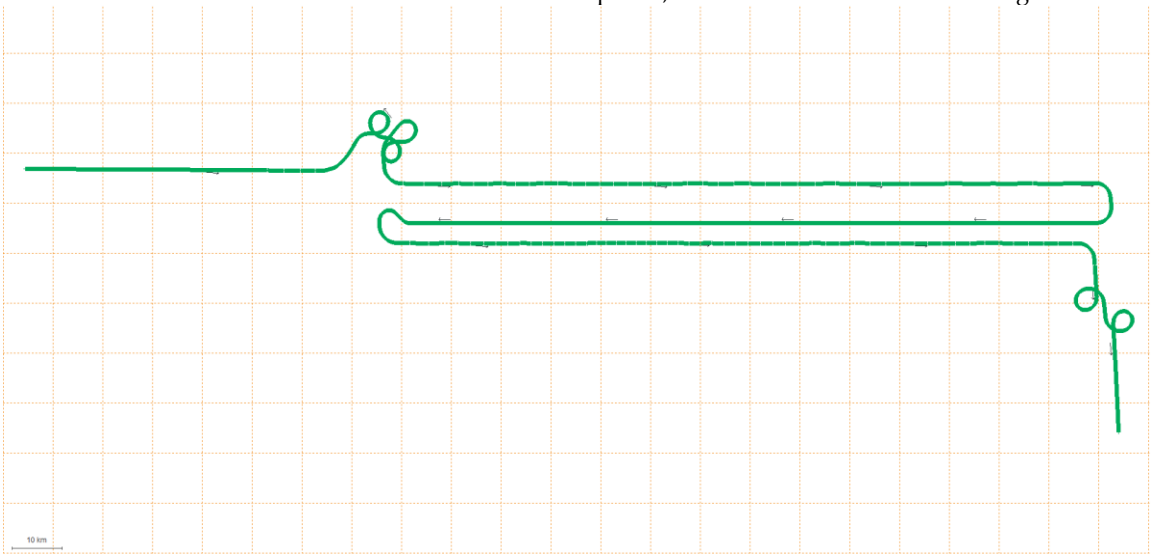

Figure S5. POS coordinates from the second flight sortie. Green dots denote individual POS coordinate points, and black arrows show the direction of flight.

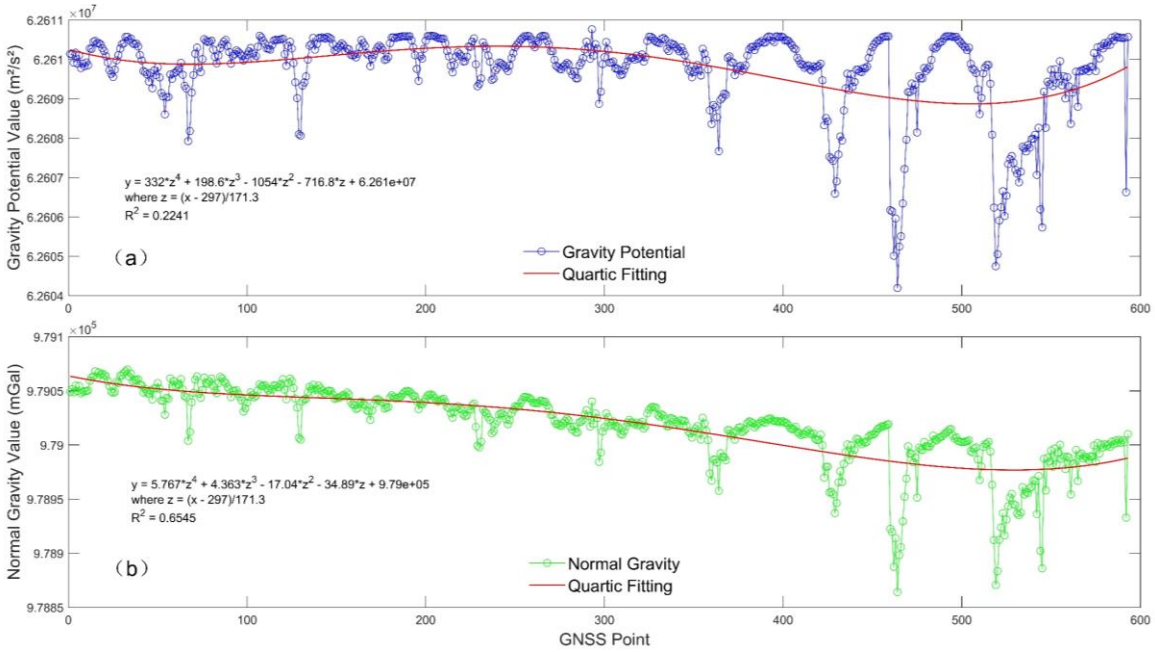

Figure S6. Gravity potential values and normal gravity values calculated using the EGM2008 model. (a) Gravity potential, (b) Normal gravity.

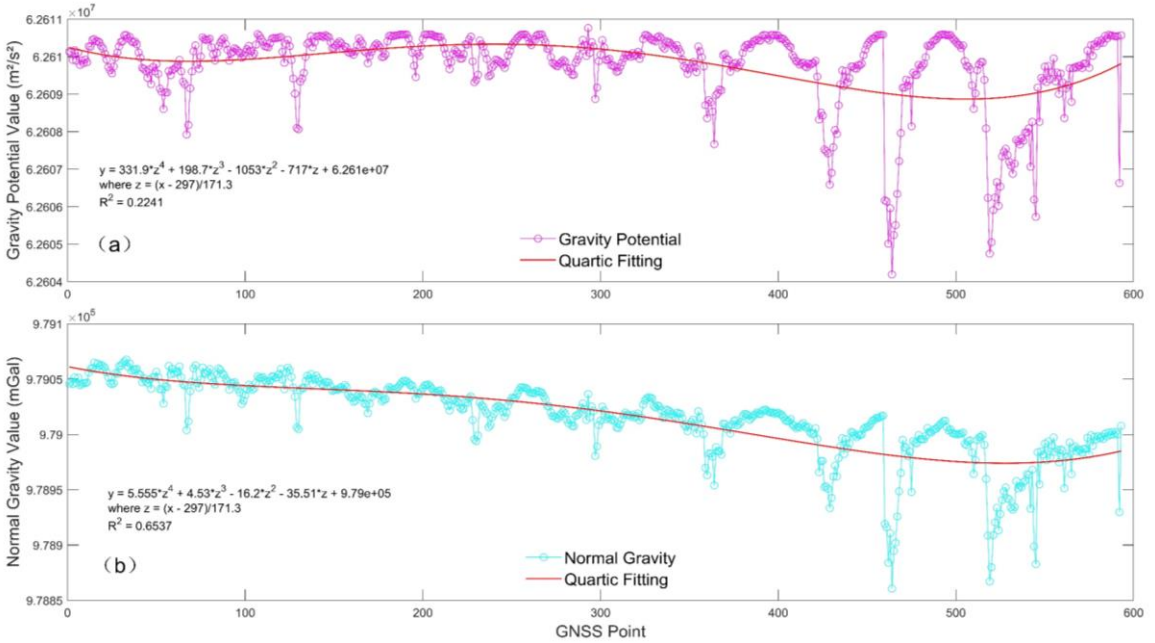

Figure S7. Gravity potential values and normal gravity values calculated using the Eigen-6C4 model. (a) Gravity potential, (b) Normal gravity.

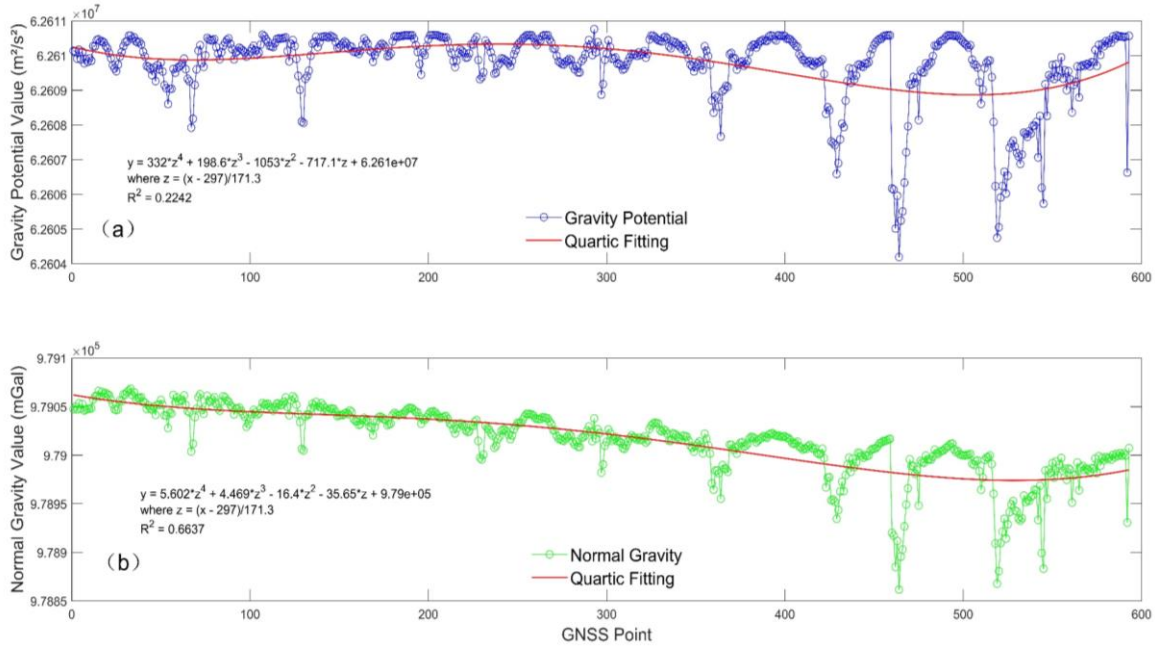

Figure S8. Gravity potential values and normal gravity values calculated using the SGG_UGM_2 model. (a) Gravity potential, (b) Normal gravity.

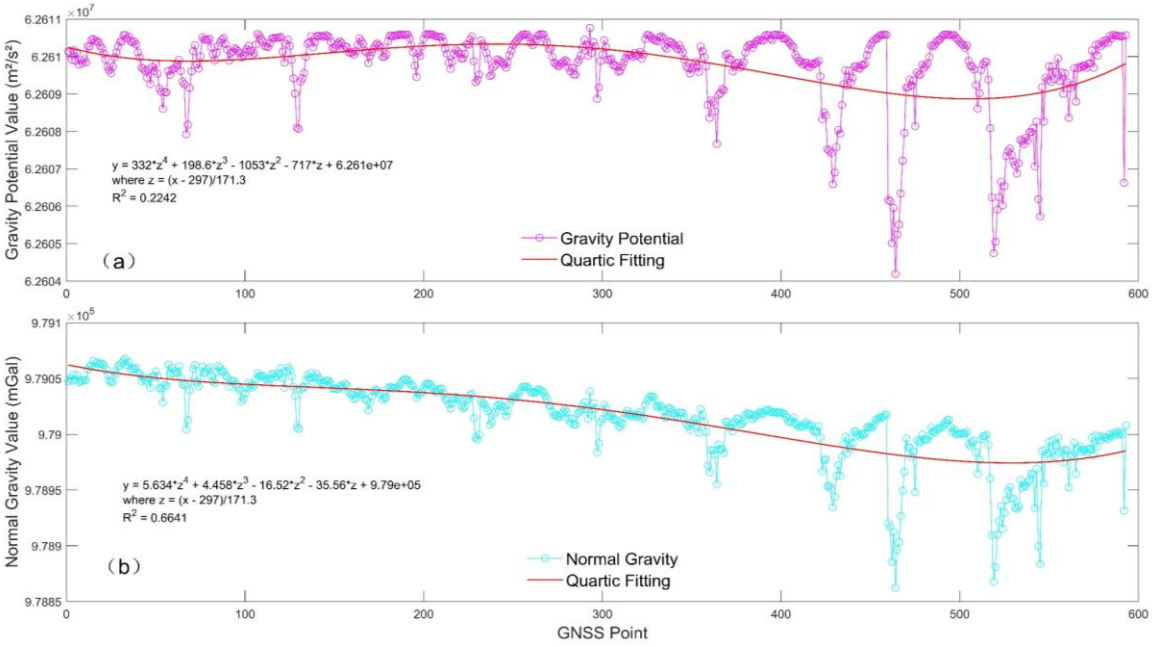

Figure S9. Gravity potential values and normal gravity values calculated using the SGG_UGM_1 model. (a) Gravity potential, (b) Normal gravity.

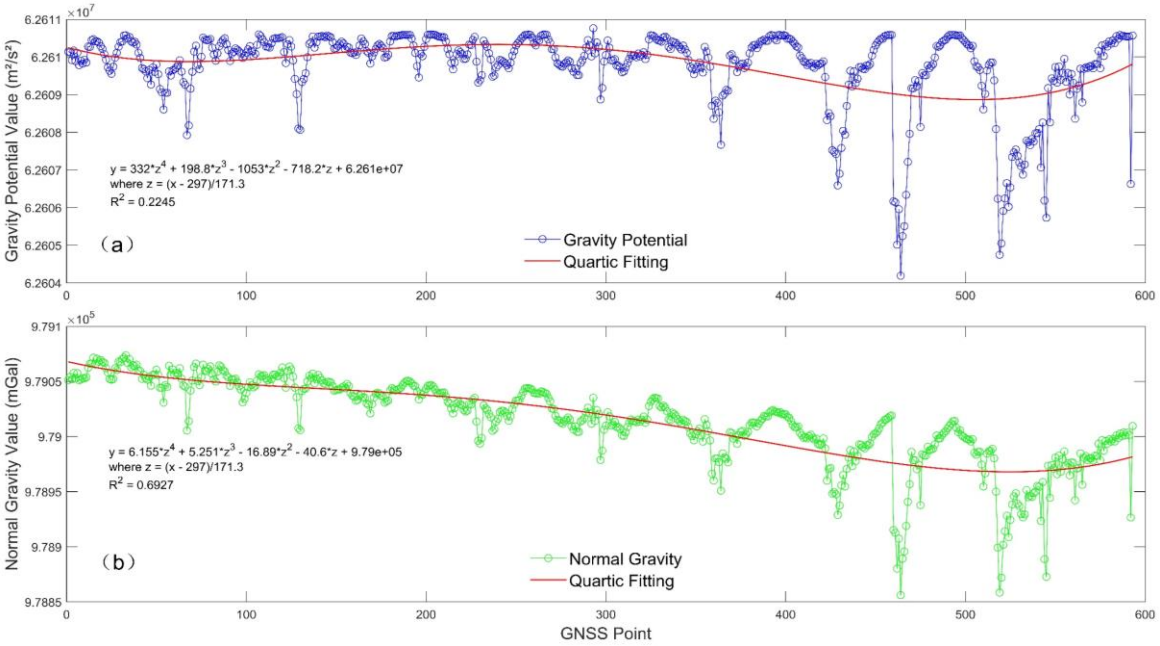

Figure 10. Gravity potential values and normal gravity values calculated using the GECO model. (a) Gravity potential, (b) Normal gravity.

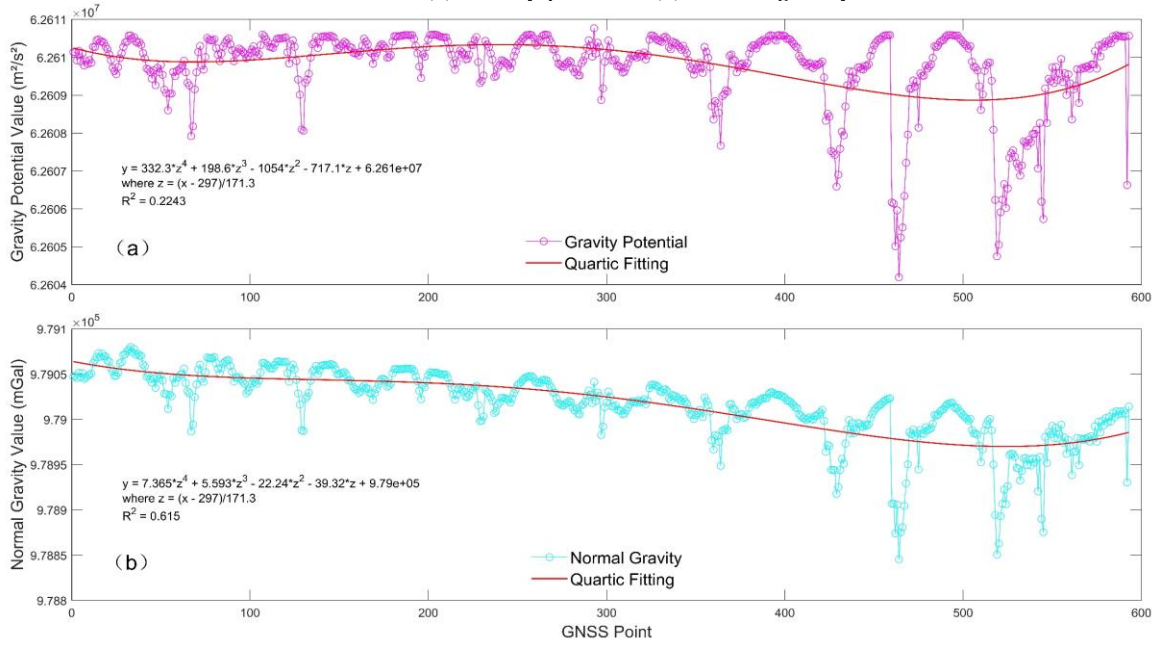

Figure 11. Gravity potential values and normal gravity values calculated using the EigenCG03C model. (a) Gravity potential, (b) Normal gravity.

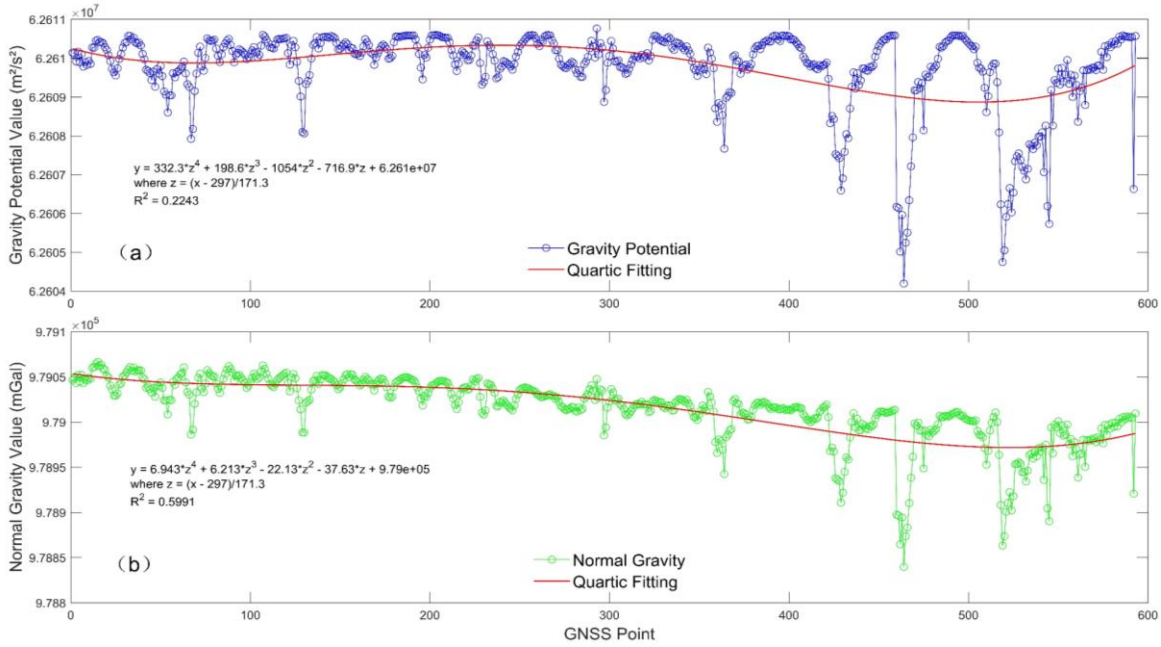

Figure S12. Gravity potential values and normal gravity values calculated using the GGM05C model. (a) Gravity potential, (b) Normal gravity.

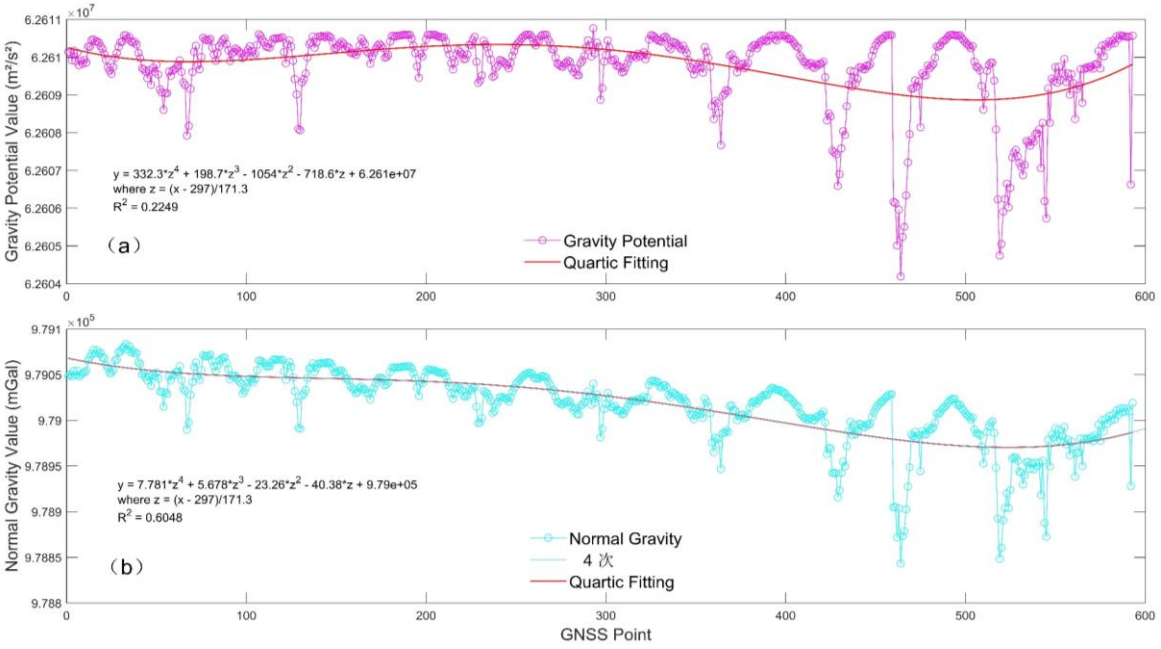

Figure 13. Gravity potential values and normal gravity values calculated using the EGM96 model. (a) Gravity potential, (b) Normal gravity.

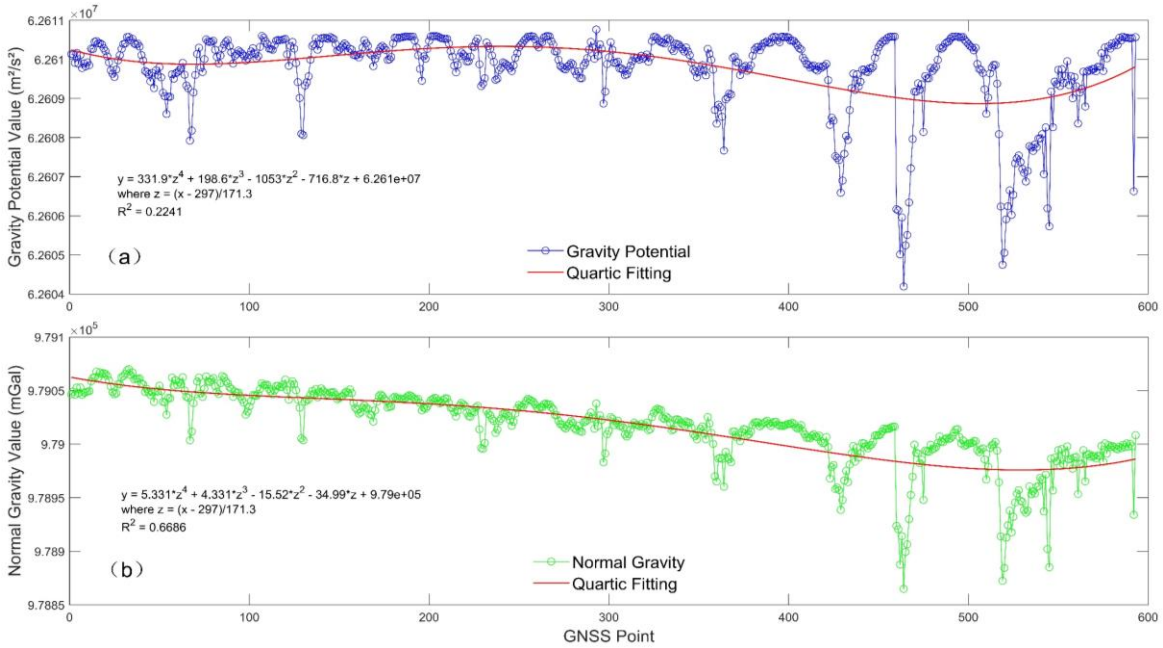

Figure S14. Gravity potential values and normal gravity values calculated using the XGM2019e-2159 model. (a) Gravity potential, (b) Normal gravity.

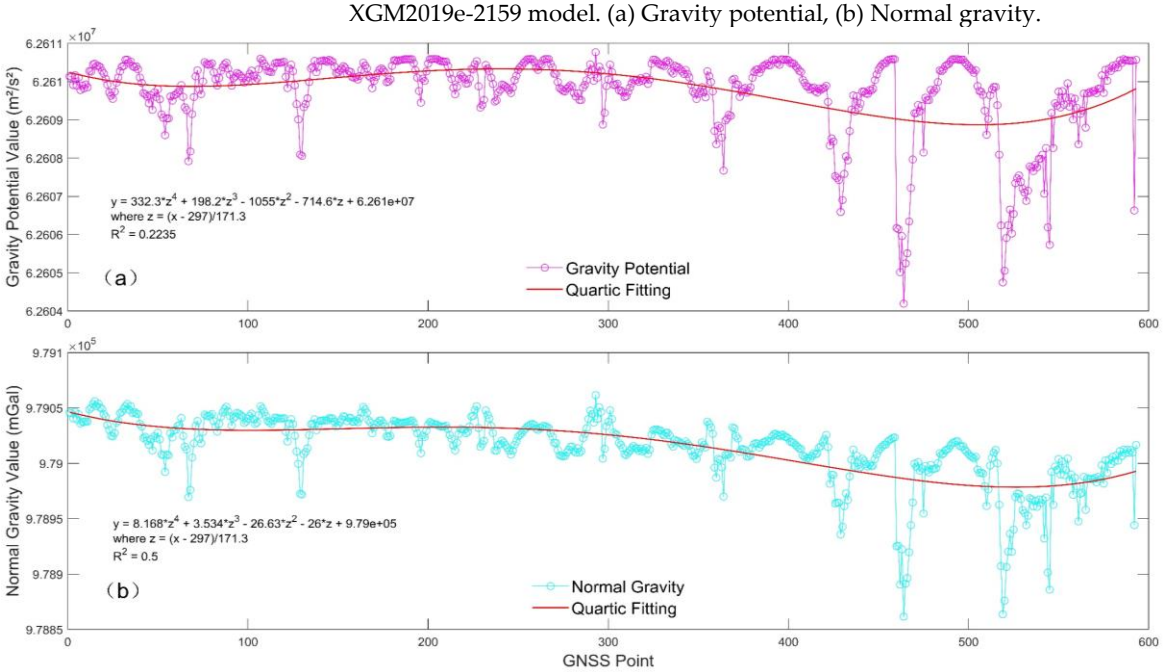

Figure S15. Gravity potential values and normal gravity values calculated using the GO_CONS_GCF_2_DIR_R6 model. (a) Gravity potential, (b) Normal gravity.

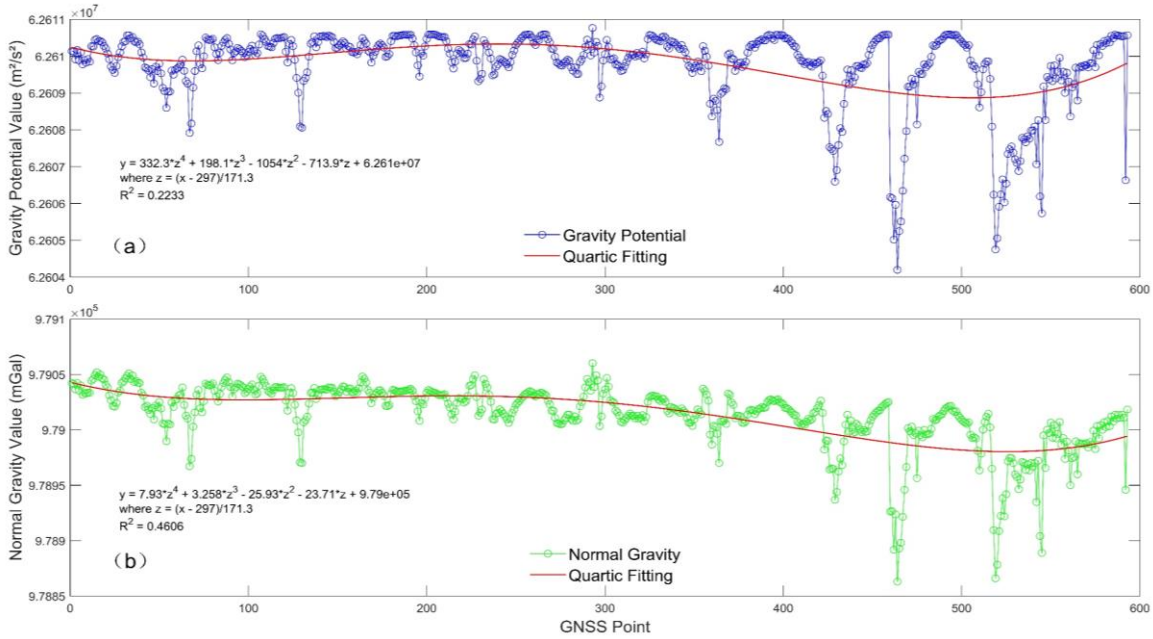

Figure S16. Gravity potential values and normal gravity values calculated using the Tongji_GMMG2021S model. (a) Gravity potential, (b) Normal gravity.

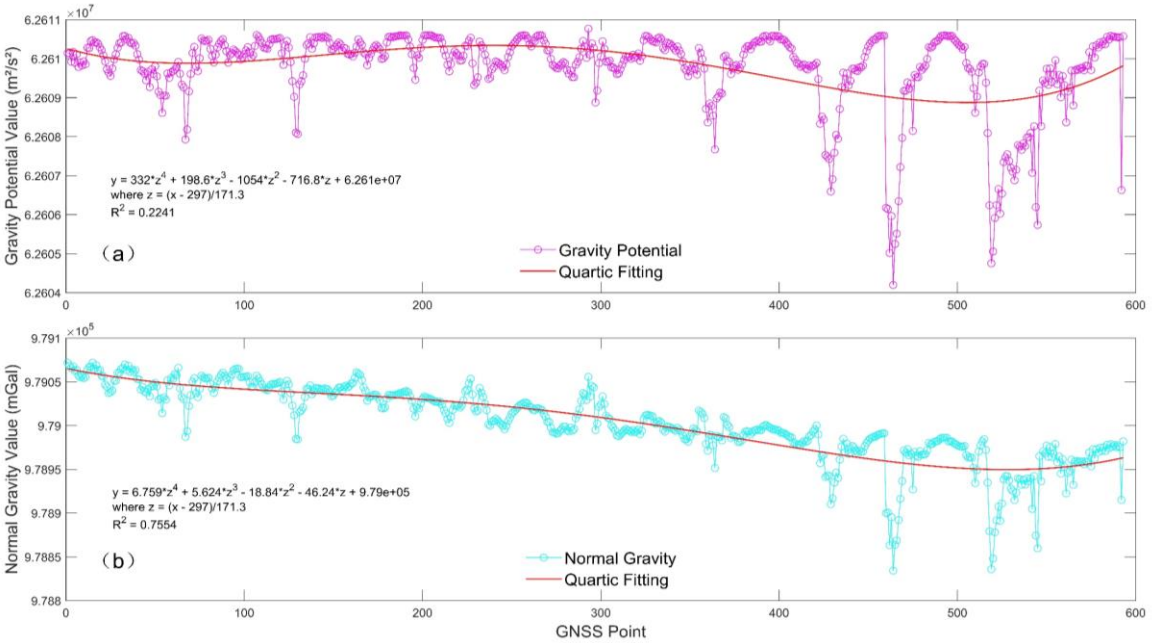

Figure S17. Gravity potential values and normal gravity values calculated using the Tongji_GRACE02S model. (a) Gravity potential, (b) Normal gravity.

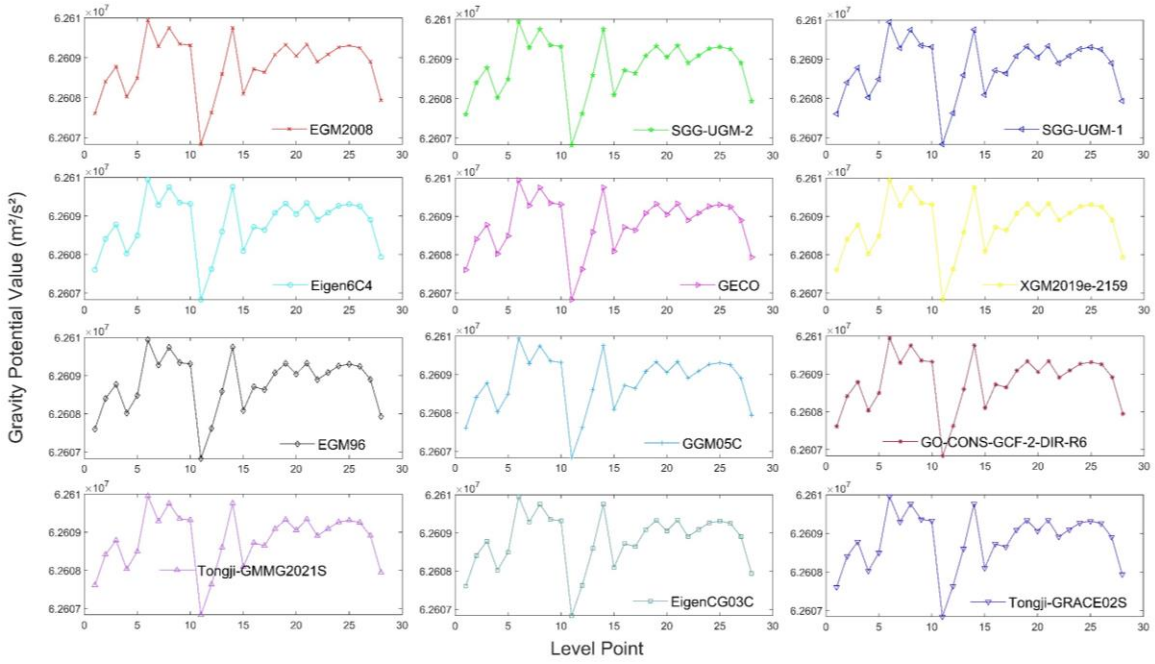

Figure S18. Gravity potential values calculated using the leveling points.

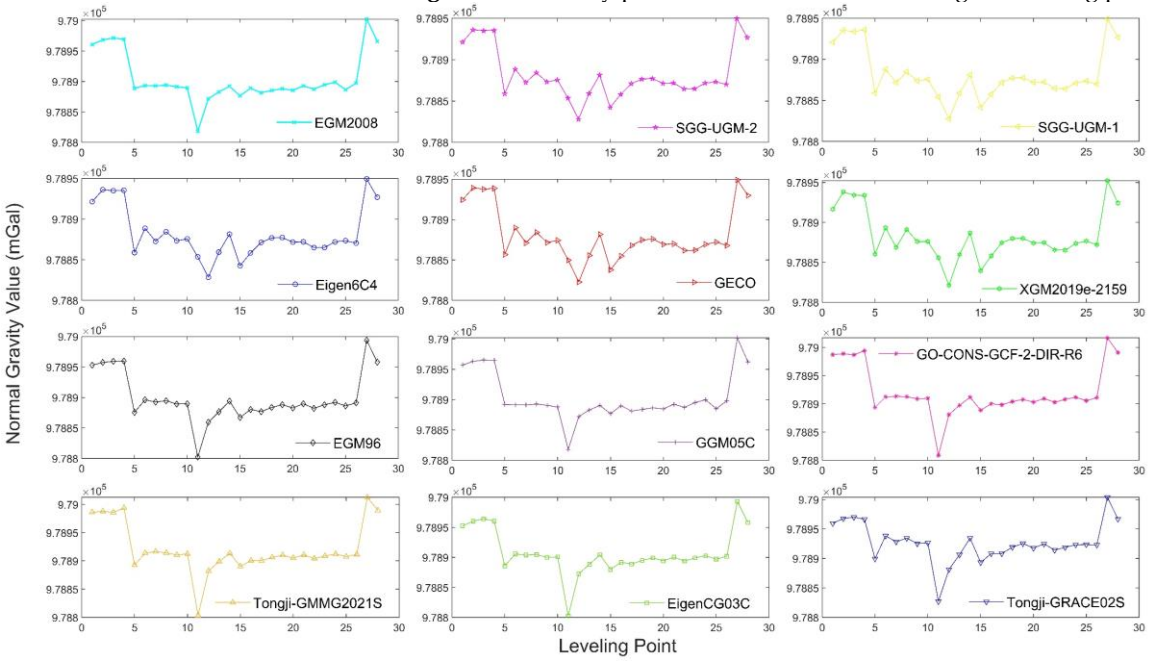

Figure S19. Normal gravity values calculated using the leveling points.

References

1. Heid, T.; Kääb, A. Evaluation of existing image matching methods for deriving glacier surface displacements globally from optical satellite imagery. Remote Sens. Environ. **2012**, 118, 339–355. [CrossRef]